



Effect of Zinc Doping on Structural, Optical, Magnetic, and Catalytic Behavior of Co_3O_4 Nanoparticles Synthesized by Microwave-Assisted Combustion Method

Chandra Sekhar Dash¹ · M. Sukumar² · V. Ravi³ · G. Anitha⁴ · Jothi Ramalingam Rajabathar^{5,7} · Khadijah Mohammedsaleh Katubi⁶ · Norah Salem Alsaieri⁶ · Khamael M. Abualnaja⁷ · R. Rajkumar¹¹ · M. Kamalakannan⁸ · M. Sundararajan⁹ · A. Sutha¹⁰

Received: 17 January 2022 / Accepted: 10 October 2022 / Published online: 28 October 2022
© The Author(s), under exclusive licence to Springer Science+Business Media, LLC, part of Springer Nature 2022

Abstract

The microwave-assisted combustion process (MCP) was adapted to prepared Zinc doped Co_3O_4 spinel nanoparticles. Scanning electron microscopy (SEM), Fourier transform infrared spectroscopy (FTIR), diffuse reflectance spectroscopy (DRS), energy dispersive X-ray analysis (EDX), X-ray diffraction (XRD), and vibrating sample magnetometer (VSM) techniques were used to investigate the structural, optical, morphological, magnetic, and catalytic properties. The cubic spinel structure was obtained without impurities in the X-ray diffraction (XRD) patterns of undoped Co_3O_4 and Zn^{2+} doped Co_3O_4 ($x=0.1$ and 0.3) respectively. However, as the Zn^{2+} concentration increased, at $x=0.5$, a new hexagonal phase appeared in addition to the cubic phase, with mean crystallite size of the cubic spinel structure extending from 48.6 to 25.5 nm. It is found that Zn^{2+} doping in Co_3O_4 matrix can induce a negative shift in the flat-band potential (VFB) and increases the isoelectric point. The Co–O stretching mode of the cubic spinel Co_3O_4 structure is responsible for the occurrence of FT-IR bands at about 662 and 573 cm^{-1} . Kubelka–Munk (K–M) method is utilized to deduce the direct band gap and decline in the band gap values (1.87–1.72 eV) observed with rise in Zn^{2+} content. TG–DTA analysis confirms the weight loss and exothermic transitions. Scanning and transmission electron microscopy were used to study the morphology and the images depicted with intragranular pores, fused grains with different grain boundaries and homogeneous distributions. The transition from paramagnetic to super-paramagnetic behavior was most likely caused by the exchange of Zn and Co ions, as well as the phase composition of ZnO (hexagonal phase) and Co_3O_4 (cubic phase). The as-fabricated Zn^{2+} doped Co_3O_4 nanoparticles were evaluated for the catalytic activity tests carried out in a batch reactor operating under atmospheric conditions. The high doping concentration (about, $x=0.5$) sample exhibited excellent catalytic activity and it exhibited better conversion efficiency and selectivity of 97.3% and 95.3%, respectively.

Keywords $\text{Co}_{1-x}\text{Zn}_x\text{O}_4$ spinel nanoparticles · Microwave combustion synthesis · Optical properties · Magnetic properties · Catalytic properties

Introduction

Nanostructure materials and spinel nanoparticles have been widely studied in the past decades due to its attractive structural, electrical and magnetic characteristics. Magnetic nanoparticles are highly polarized with an electronic spin, resulting in 80% of high magneto-resistance at room temperature [1, 2]. Currently, the synthesis of electrochemical, magnetic, catalytic, optical, mechanical, and thermal properties of cobalt oxide formed excessive concentration due to its various technological applications, such as contain magnetism, solid-state sensors, lithium-ion batteries, heterogeneous

✉ M. Sukumar
msukumsc@gmail.com

✉ Jothi Ramalingam Rajabathar
jrajabathar@ksu.edu.sa

✉ M. Sundararajan
sundar15msc@gmail.com

Extended author information available on the last page of the article

catalysts, gas sensors, energy storage, solar energy absorbers, particularly in super capacitors, because of its higher surface area, and electrochemical devices [3–5].

Co_3O_4 is a widely used magnetic material that has piqued the interest of researchers in electrolysis, which is shown to exhibit remarkable photo-electrochemical properties due to an excellent stability (in alkaline media) during oxygen redox processes and provides promising redox potential abilities [6–8]. Co_3O_4 and/or Co-based nano-composite materials an enhancement agent for magnetic resonance imaging or correspondingly offers stimulating benefits on several engineering and medicine (drug delivery application) [6, 8]. Co_3O_4 is a transition (binary) metal oxide with cubic normal spinel crystal structure and one of the important and attractive *p*-type semiconductors with anti-ferromagnetic material with Neel temperature (T_N) of ~ 30 K [3, 9, 10]. The anti-ferromagnetic ordering of Co_3O_4 is caused by super-transfer interactions, which may occur via two positive path ways, for example (i) $\text{Co}^{2+}\text{--O--Co}^{3+}\text{--O--Co}^{2+}$, (ii) $\text{Co}^{2+}\text{--O--Co}^{2+}$ [3]. The cobalt oxide has an essential narrow band gap of 0.74 eV, which is far narrower than the commonly agreed band gap values ranging from 1.5 to 2.5 eV, and this band gap value is derived from a simple dipole prohibited d–d transition between tetrahedral-site Co^{2+} cations [7, 11]. Cobalt oxides are formed in a variety of oxidation states, which makes the materials attractive. The composite might occur in the form of the rock salt structure of cobalt (II) oxide (CoO). Alternatively, spinel cobalt (II, III) oxide (Co_2O_3 and Co_3O_4), fabricated by a process of mixed oxidation (Co^{2+} and Co^{3+}) state [8]. It is well known that magnetic Co^{2+} ions occupy the tetrahedral sites as Co_3O_4 crystallizes in the cubic natural spinel form, while the non-magnetic Co^{3+} ions occupy the octahedral sites [5]. Cobalt oxide nanoparticles as one of the fascinating magnetic properties, it has greater attention owing to its uses in supercapacitor [12], lithium-ion battery [13], gas sensor [14], heterogeneous catalyst [15], and so on. This has been widely analyzed as steady catalysts for oxygen reduction reaction (ORR) and oxygen evolution reaction (OER) because of its lower price [16]. The oxides are common in nature, and only CoO and Co_3O_4 are stable, with Co_3O_4 having the greatest steadiness of all of the cobalt oxides.

Various methods have been used to create magnetic cobalt oxide nanoparticles such as sol–gel [17], chemical vapor deposition [18], sonochemical [19], spin coating [20], spray pyrolysis [21], solid-state thermal decomposition method [22], mechano-chemical reaction [23], precipitation [24], hydrothermal [25] are some of the general synthesizes methods used for Co_3O_4 . These methods, however, either take time or require costly instruments. In such situations, the synthetic route with microwave assisted is an appropriate approach; the narrow size distribution and high purity are the additional advantages [10].

However, there are few studies on the synthesis of ZnO and Co_3O_4 using MCP. This work emphases on the preparation of Zn^{2+} doped Co_3O_4 using MCP. The outcome of Zn^{2+} doping on Co_3O_4 using microwave effect for secondary (ZnO at $x=0.5$) appearance is explored. Zn^{2+} is doped with Co_3O_4 nanoparticles owing to its good conductivity, thermo chemical stability and low manufacture price. ZnO is an inherently n-type semiconductor with a 3.37 eV optical band gap and a high exciton binding energy of 60 meV [9].

The present work aims to exploit the preparation methodology of Co_3O_4 and doping Zn^{2+} in Co_3O_4 nanoparticles and various physical characterization techniques are employed to study the structural, optical, thermal, surface morphology and magnetic characteristics are studied in detail and elaborated in the subsequent sections. The as-prepared undoped cobalt oxide and zinc doped cobalt oxide nanoparticles have also been assessed for the glycerol oxidation to discover their possible catalytic application.

Experimental

Materials

The chemicals such as cobalt nitrate, zinc nitrate and L-alanine of analytical grade (99.9%), obtained from SD Finechemicals, India. The chemicals were used directly without performing any extra purification. Double distilled water is utilized during the process of sample preparation.

Synthesis of Zn^{2+} Doped Co_3O_4 Nanoparticles

Appropriate amounts of cobalt nitrate, zinc nitrate (precursors-oxidizers), and L-alanine (fuel) were utilized in the microwave combustion technique to create spinel nanoparticles. The fuel-to-oxidizer (F/O) ratio retained at 1 as per the principle of propellant chemistry [2]. The standard procedure, extracted homogeneous solution (precursors), was dissolved in de-ionized water and stirred for 45 min at 300 K. In a microwave (800 W), which operates at 2.45 GHz, the homogeneous solution was introduced for a short period of 15 min. The precursor solution was dehydrated and combusted after reaching the threshold temperature and the black fluffy powder as obtained was calculated at 550 °C for 2.5 h. The attained samples were processed at a stoichiometric concentration, $\text{Co}_{1-x}\text{Zn}_x\text{O}_4$ with $x=0, 0.1, 0.3$ and 0.5 were labeled as (a), (b), (c) and (d), respectively.

Characterizations

The thermogravimetric behavior of the as-prepared powders was examined using an Exstar TG/DTA 7200 instrument from SII Nanotech at a heating rate of 5 °C min^{-1} in

a nitrogen atmosphere. X-ray diffraction (Rigaku Model Smartlab 3 kW X-ray diffractometer) in 2 θ scale 10–80° fitted with Cu K radiation = 1.5406 Å was used to define the structural properties of the as-prepared powders. Thermo Scientific make NICOLET iS10 is utilized to perform FTIR studies and to determine function classes. In order to study optical characteristics Evolution 300 UV–visible spectrophotometer of Thermo Scientific make is used at RT. HITACHI S4800 equipped with EDS of HORIBA EMAX make was employed to perform morphological studies and to confirm elemental composition. A PMC Micro Mag 3900 type VSM equipped with a 1 T magnet is used to study magnetization curves at RT.

Catalytic Activity

The catalytic conversion of glycerol was carried out in a batch reactor operating under atmospheric conditions using a two-necked round bottom flask (250 ml) equipped with reflux condenser and temperature controller. The starting mixture containing zinc doped cobalt oxide catalysts (50 mg), glycerol (C₃H₈O₃) as reactant (0.05 mol), hydrogen peroxide (H₂O₂) as oxidant (0.05 mol) and dimethyl sulfoxide (DMSO) as solvent, was placed in a two necked round bottom flask equipped with a water condenser. The temperature was maintained at 80 °C for 390 min (6.5 h) and then cooled down to 304 Kelvin. The oxidized products were analyzed by gas chromatography (GC) with flame ionization detector, using a MAYURA 1100. The main by-products were confirmed by gas chromatography mass spectrometer (GC–MS) using Agilent Technologies Model 7890A.

Results and Discussion

Structural Analysis

The development of X-ray diffraction (XRD) patterns as a result of Zn²⁺ doping material is seen in Fig. S1. Pure Co₃O₄ and Zn_{0.1}Co_{0.9}O₄, Zn_{0.3}Co_{0.7}O₄ samples show typical peaks of a single phase with a cubic structure and a space group

$Fd\bar{3}m$, in accordance with JCPDS card No: 43-1003). No other peaks have been noticed; this implies that microwave combustion method, followed by 2.5-h calcination at 550 °C, is adequate to prepare a single phase Co₃O₄ nanoparticles. The characteristics peaks at about 2 θ values 19.0°, 31.2°, 36.8°, 38.5°, 44.8°, 59.3°, 65.2° are (111), (220), (311), (222), (400), (511), and (440) crystallographic planes, correspondingly. However, with increase in Zn²⁺ concentration $x=0.5$, the new secondary ZnO phase (space group $P63mc$) with hexagonal structure (the characteristics peaks at 2 $\theta \approx$ 32.1° (100), 34.8° (002), 36.6° (101), 57.0° (110), 63.3° (103), 68.2° (112)) looks, in accordance with JCPDS No. 75–1526. It was found that higher doping concentration $x=0.5$ (Zn_{0.5}Co_{0.5}O₄), a new secondary ZnO hexagonal process occurs. As Co²⁺ ions are replaced by Zn²⁺ ions, two phase-systems with cubic (Co₃O₄) and hexagonal (ZnO) structures form, suggesting the forming of a composite. The amplitude of the peak corresponding to the hexagonal step is observed to decrease as Zn²⁺ concentration increases.

The Debye–Scherrer formula was used to calculate the average crystallite size (D) of Zn²⁺ doped Co₃O₄ [26].

$$D = \frac{0.89\lambda}{\beta \cos \theta}, \quad (1)$$

where, λ is the wavelength of an X-ray, β is the full width at half maximum (FWHM) and θ is the Bragg diffraction angle. The reported results show that the average crystallite size of undoped cobalt oxide is 48.6 nm, while for Zn²⁺ doped samples it has been detected slightly smaller range 42.9–25.5 nm as shown in Table 1. Increased substitutions of Zn²⁺ concentrations resulted in a haphazard decrease in the crystallite size of Co₃O₄ nanoparticles.

The XRD patterns were used to quantify the lattice parameters of a Zn²⁺ doped Co₃O₄ method using Eq. (2)

$$\frac{1}{d^2} = \frac{h^2 + k^2 + l^2}{a^2}, \quad (2)$$

where h , k , and l are the miller indices, a is the lattice parameter, and d is the inter-atomic spacing. Table 1 depicts the cubic phase's lattice parameter and unit cell number.

Table 1 Structural parameters and energy gap of Zn²⁺ doped Co₃O₄ nanoparticles

| Sample Code | 2 θ (°) | FWHM, β (Å) | Average Crystallite size D (nm) | Lattice Parameter, a (Å) | Cell volume (Å ³) | Micro-strain, ϵ (Å) | Lattice strain, ϵ ($\times 10^{-14}$) (lin ⁻² m ⁻⁴) | Dislocation density, δ ($\times 10^3$) (lin ⁻² m ⁻²) | Energy gap (eV) |
|-------------|----------------|-------------------|-----------------------------------|----------------------------|-------------------------------|------------------------------|---|--|-----------------|
| (a) | 37.04 | 0.170 | 48.6 | 8.0515 | 521.96 | 7.282 | 7.047 | 26.998 | 1.87 |
| (b) | 36.99 | 0.193 | 42.9 | 8.0566 | 522.95 | 8.269 | 7.988 | 34.649 | 1.82 |
| (c) | 36.97 | 0.242 | 34.2 | 8.0600 | 523.60 | 10.369 | 10.018 | 36.367 | 1.78 |
| (d) | 36.93 | 0.324 | 25.5 | 8.0632 | 524.23 | 13.910 | 13.425 | 97.946 | 1.72 |

However, lattice constant increases with increasing x value. The diffraction peaks (311) shift toward a lower angle as the concentration of Zn^{2+} increases. The shift in peak position between the samples with a Zn^{2+} doping level from $x=0$ to 0.5 is $\Delta\theta=0.11^\circ$, indicating that the lattice constant increased from 8.0515 to 8.0632 Å. This variation can be attributed to the greater ionic radius Zn^{2+} ($r_{\text{Zn}^{2+}}=0.074$ nm at tetrahedral coordination) ions strengthened the lattice parameter compared to the comparatively smaller ionic radius Co^{2+} ($r_{\text{Co}^{2+}}=0.072$ nm at tetrahedral coordination) ions [27].

In addition, the micro-strain (ϵ), lattice strain (ϵ) and dislocation density (δ) are also calculated using Eqs. (3), (4) and (5) respectively. [28]

$$e = \frac{\beta}{4 \tan \theta} \quad (3)$$

$$\epsilon = \frac{\beta \cos \theta}{4} \quad (4)$$

$$\delta = \frac{15\beta \cos \theta}{4aD} \quad (5)$$

Table 1 summarizes the comprehensive structural parameters for the (311) peak, demonstrating that as doping concentration increases, the crystallite size decreases while the micro-strain, lattice strain, and dislocation density increase, owing to doping greater ionic radius (Zn) into lesser ionic radius (Co).

Zeta Potential

Zeta potential measurements were used to investigate the surface changes of the materials. Figure 1 depicts the variation of zeta potential with pH in aqueous suspensions. The zeta potential results show that the particle surface charge of undoped and Zn^{2+} doped Co_3O_4 nanoparticles in ethanol medium ranged from +19 to +25 mV and -16 to -21 mV, respectively. These findings showed that the as-prepared nanoparticles were relatively stable in an aqueous suspension. Because of the high zeta potential, the undoped and Zn^{2+} doped Co_3O_4 material suspensions were more stable in alkaline medium. In general, nanoparticles with zeta potentials around 30 mV (-ve or +ve) demonstrated excellent colloidal stability. In contrast, the isoelectric point of the pure and Zn^{2+} doped Co_3O_4 nanoparticles increases from 5.3 to 6.1, preferring glycerol oxidation [29–31].

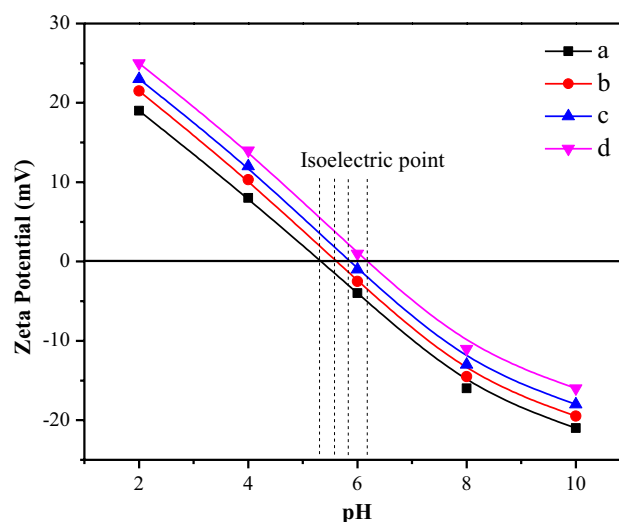


Fig. 1 The pH-dependent zeta-potential of the pure and Zn^{2+} doped Co_3O_4 nanoparticles

Optical Properties

The UV-DRS study is performed on the zinc doped cobalt oxide samples to determine the optical characteristics in the wavelength range of 200–800 nm. In the evaluation of the optical energy band gap the diffuse reflection research plays a major role. It is extracted utilizing the modified Tau'c relation [32] as given by Eq. (6):

$$F(R)h\nu = A(h\nu - E_g)^n, \quad (6)$$

where $n=1/2$ and 2 for direct and indirect transitions, respectively, as a result, direct and indirect band gaps are created. The Kubelka–Munk (K–M) function $[F(R)]$ is commonly used to transform diffuse reflectance into the corresponding absorption coefficient, as seen in Eq. (7), and is primarily utilized for investigating powder samples:

$$\alpha = F(R) = \frac{(1 - R)^2}{2R} \quad (7)$$

A graph is drawn between $[F(R)h\nu]^2$ and $h\nu$, and the linear regions of these graphs are extrapolated to $[F(R)h\nu]^2=0$ to yield the direct band difference values as shown in Fig. S2. The estimated band gap values of Zn^{2+} doped structure is noted to be 1.87, 1.82, 1.78, and 1.72 eV (Table 1) for $x=0, 0.1, 0.3,$ and 0.5 respectively. However, increasing the Zn^{2+} doping causes a decline in the band gap value; i.e., 1.87–1.72 eV for un-doped to 50% Zn^{2+} addition. The contraction in band gap with doping of Zn^{2+} ions is seen owing to the creation of sub-bands amid the energy band gap. Further, combination of these sub bands with the conduction band results in the formation of continuous band, thereby lowering the band gap value [33].

FTIR Analysis

Fig. S3 depicts the FTIR spectra of zinc doped cobalt oxide logged in the 4000–400 cm⁻¹ region. The FT-IR spectral analysis was carried out to observe the development of nanostructure and the existence of surface functional groups. The bands associated with higher wavenumbers are mapped with H, O, and C bonds. Wide band at 3444 cm⁻¹ is linked to the O–H longitudinal stretching vibration of adsorbed water molecules. The band at 2914 cm⁻¹ are aligned with the C–H symmetric and asymmetric stretching sensations. Further, existence of a band at 1624 cm⁻¹ confirms the occurrence of (H–O–H) bond vibration. Consequently, owing to the adopted combustion path of material synthesis, a weak band is seen at 1380 cm⁻¹, which corresponds to the remaining nitrogen groups. The symmetric stretching of CO₃²⁻ ion is allotted to the weak band at 1040 cm⁻¹. The fingerprint stretching vibrational modes of Co–O bonds is confirmed by observation by two distinct, sharp bands at 662 and 573 cm⁻¹, which ensures the formation of the cubic Co₃O₄ nanoparticles [34]. However, the increasing Zn²⁺ doping content at $x=0.5$, the presence of band at 479 cm⁻¹ corresponds to the stretching vibrational mode of hexagonal ZnO bond [35], which proved the high crystallinity of the sample as evidenced from XRD ($x=0.5$) analysis.

TG/DTA Analysis

Thermogravimetric analysis was performed on the zinc doped cobalt oxide nanoparticles. The TG/DTA curves of the zinc doped system of the samples are given in Fig. S4. The initial stage of weight loss was noted to be 0.3, 0.1, 0.15 and 0.3% ($0 \leq x \leq 0.5$) between 50 and 218 °C, and further dehydration of H₂O molecules which is present on the particle surface is observed due to the existence an endothermic peak in the DTA thermogram. The next stage of weight loss was observed to be 0.12, 0.1, 0.4 and 0.31% ($0 \leq x \leq 0.5$) occurring between 242 and 400 °C is due to the decay of the organic compound, removal of hydroxyl group and volatile components existing in the prepared sample. No weight loss was noticed after 400 °C, this may be due to institutional reorganization. As a result, calcination has been carried out at the temperature above 400 °C, which indicates the thermal stability of zinc doped cobalt oxide nanoparticles [36, 37].

SEM Study

The surface morphology of the as prepared Zn²⁺ doped cobalt oxide is depicted in Fig. S5, combustion route entails the outflow of water molecules and volatile gases (O₂, N₂, and CO₂), resulting in the development of a simple nanostructure with varying degrees of porosity. Upon visual inspection the obtained images confirmed the formation of

the porous nanosized crystallized grains. Further the presence of fused grains with discrete grain boundaries served as origin point for pore walls and several small-sized isolated grains with pores. Energy dispersive X-ray (Fig. S6) analysis has been used to determine the elemental conformation of the Zn²⁺ doped Co₃O₄ nanoparticles and the existence of Co/Zn and O elements were verified, and the respective fraction of elemental composition is shown in the inset table of Fig. S6.

TEM Study

Figure 2a, b illustrates transmission electron microscopy (TEM) images of undoped and Zn²⁺ ($x=0.3$) doped Co₃O₄ nanoparticles, respectively. The as-prepared nanoparticles possess spherical morphology with some degrees of agglomeration. The average grain size particles in the Zn²⁺ ($x=0.3$) doped Co₃O₄ nanoparticles clearly decreases when compared to the pure Co₃O₄ nanoparticles (51 to 36 nm), which is consistent with the size estimated from the Debye–Scherrer equation from XRD. Figure 2c is selected area diffraction (SAD) pattern from the particles confirming the presence of the Zn²⁺ doped Co₃O₄ nanoparticles. The rings are broadened considerably, indicating the nano-crystalline nature of the particles.

Magnetic Properties

The magnetization (M) vs field (H) hysteresis plot for zinc doped cobalt oxide system is shown in Fig. 3 it shows para and super-paramagnetic behavior (Table 2) at room temperature. Under the impact of magnetic field, the magnetization of the materials begins to saturate, and para to super-paramagnetic activity becomes dominant. The cobalt oxide nanoparticles were normal spinel structure, as cobalt (II) divalent and cobalt (III) trivalent metal ions occupy the tetrahedral and octahedral sites, respectively. The undoped Co₃O₄ exhibited paramagnetic behavior at room temperature, and it undergoes the weak exchange interaction between anti-ferromagnetism and ferromagnetism for surface effect below the Neel temperature at approximately 40 K. The interaction of antiferromagnetic strength is weak, that employed in unit cell all the spin-up Co²⁺ ion has tetrahedral coordination with nearest neighbor atom Co²⁺ ion with the spin down configuration [38, 39]. The corresponding undoped Co₃O₄ spinel nanoparticle is observed the saturation magnetization values (M_s) 5.8079 memu g⁻¹. Although bulk cobalt oxide material is anti-ferromagnetic behavior, this change in magnetic property due to the finite size effects [40]. As increasing Zn²⁺ ion concentration from $x=0.1$ to 0.5 are exhibited only super-paramagnetic behavior. These samples are found to non-saturate the magnetization event at the maximum applied field of 15 kOe. The undoped Co₃O₄

Fig. 2 **a, b** TEM images of pure and Zn ($x=0.3$) doped Co_3O_4 nanoparticles, respectively. **c** SAD pattern of Zn ($x=0.3$) doped Co_3O_4 nanoparticles

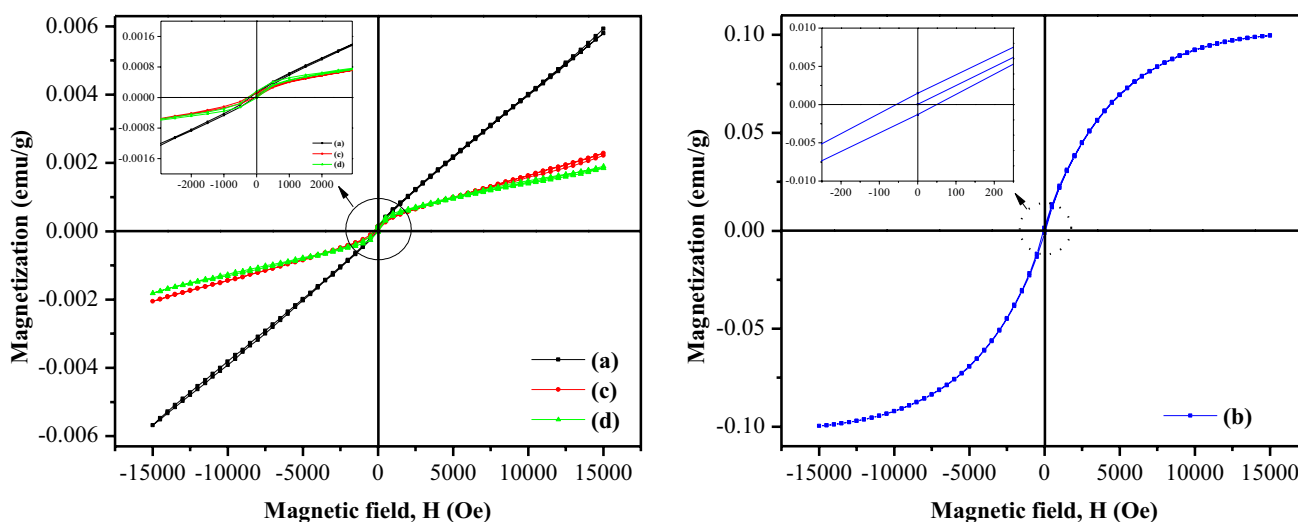
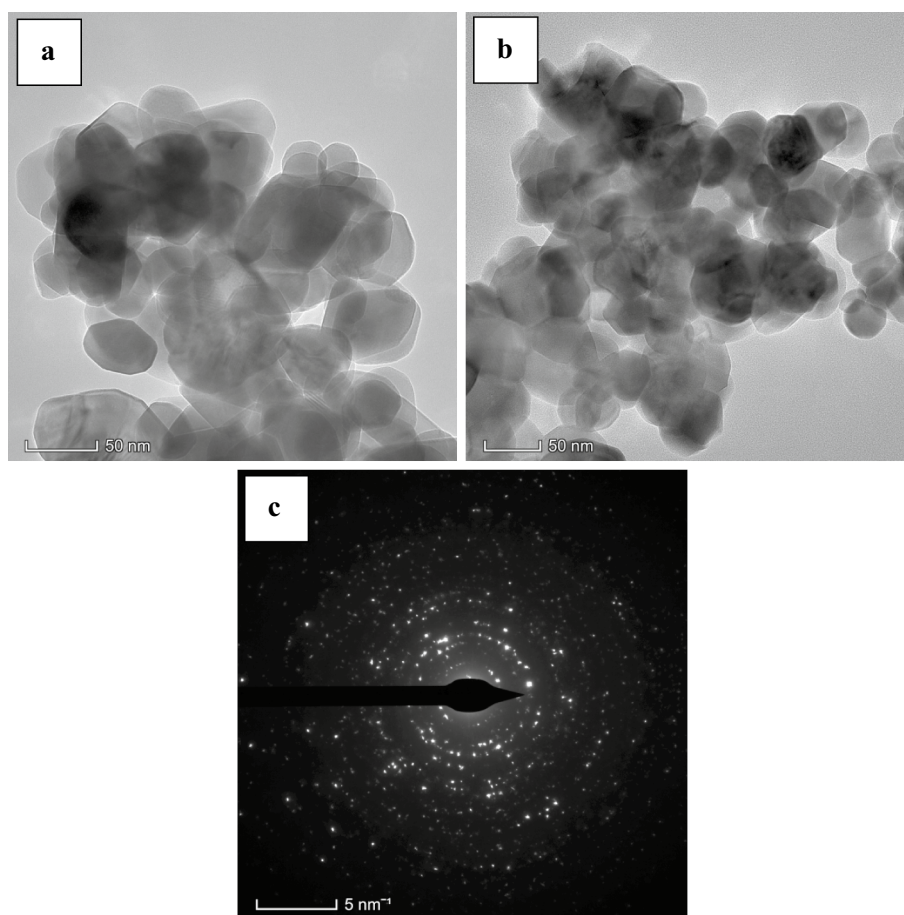


Fig. 3 Magnetic hysteresis curves of the Zn^{2+} doped Co_3O_4 nanoparticles

belong to paramagnetic materials and Zn^{2+} doped Co_3O_4 samples present weak ferromagnetic property as shown in Table 2 [41–43]. These samples corresponding to the saturation magnetization values (M_s) 99.695 to 1.8562 $\mu\text{emu g}^{-1}$. The coercivity (H_c) and remanence magnetization (M_r)

was observed that it varies with increasing Zn^{2+} concentration, which ranges from 52.871 to 135.49 Oe and 53.299 to 1395.8 $\mu\text{emu g}^{-1}$ (Table 2). These values remained to be dependent on crystallite size and shape of undoped and doped cobalt oxide nanoparticles [44].

Table 2 Magnetic properties of Zn²⁺ doped Co₃O₄ nanoparticles

| Sample Code | Magnetic behavior | Coercivity H_c (Oe) | Remanence M_r ($\mu\text{emu/g}$) | Saturation Magnetization M_{s^*} (memu/g) |
|-------------|-------------------|-----------------------|---------------------------------------|--|
| (a) | Para | 73.653 | 49.043 | 5.8079 |
| (b) | Ferro* | 52.871 | 1395.8 | 99.695 |
| (c) | Ferro* | 102.84 | 53.299 | 2.1720 |
| (d) | Ferro* | 135.49 | 87.110 | 1.8562 |

*dWeak ferromagnetic behavior

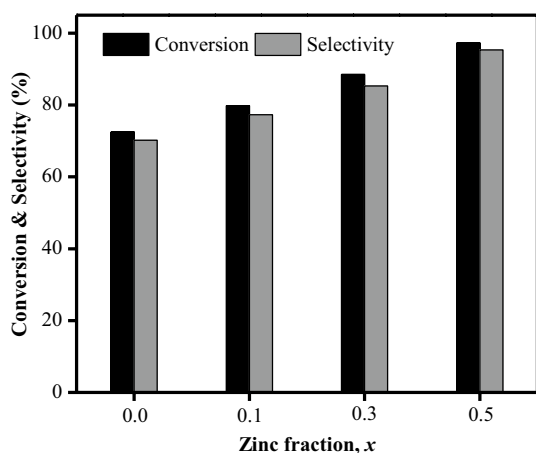
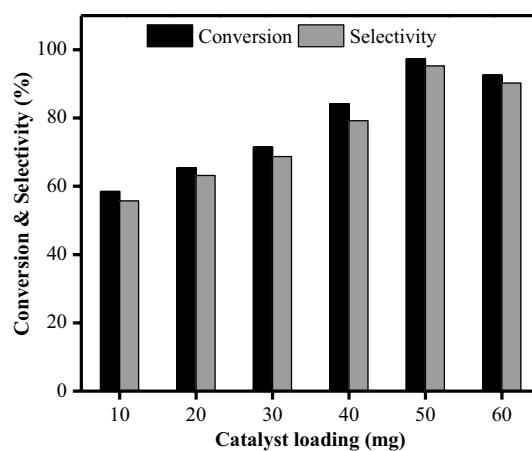
Catalytic Activity

Effect of Sample Composition

Zinc doped cobalt oxide nanoparticles have been used for the oxidation of glycerol in liquid phase batch reactor at atmospheric conditions. Increasing Zn²⁺ concentration ($x=0$ to 0.5), the catalytic conversion of glycerol increased from 77.9% to 97.3% and selectivity of formic acid increased (as observed for GC–MS results shown in Fig. S7) from 68.8% to 95.3% respectively. This catalyst ($x=0.5$) exhibits highest catalytic activity for the conversion of glycerol to formic acid as shown in Fig. 4. Thus, zinc ($x=0.5$) doped cobalt oxide catalyst alone was selected for further studies.

Effect of Catalyst Loading

Figure 5 display the effect of catalyst loading on the conversion of glycerol and product selectivity using zinc ($x=0.5$) doped cobalt oxide catalyst at 80 °C for 6.5 h and the optimum reaction condition which maximized the production of formic acid from glycerol. The conversion and the selectivity's of formic acid was the highest (97.3% and 95.3%) for 50 mg of catalyst loading. At high amount of catalyst, the conversion and the

**Fig. 4** Effect of sample composition**Fig. 5** Effect of composite loading on the conversion of glycerol over Zn²⁺ ($x=0.5$) doped Co₃O₄ catalyst

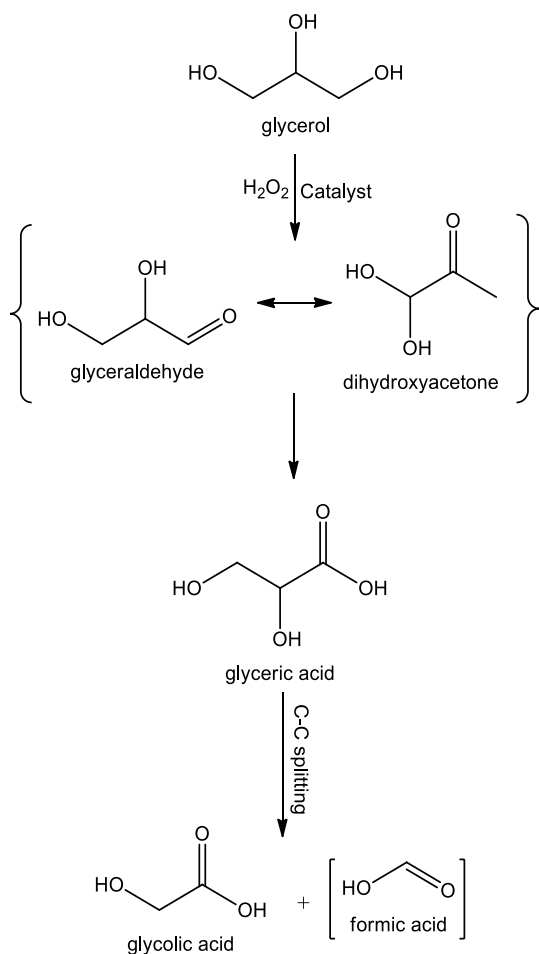
selectivity's decrease (92.6% and 90.2%) which is due to the blocking of the pore on the catalyst surface, which in turn leads to drop in the reactive surface available to head the reaction [45].

Recycling Performance

The recyclability and recoverability of $x=0.5$ sample of the nanoparticles were examined over five runs recycling test of glycerol oxidation as shown in Fig. S8. After the first reaction, the catalyst was filtered and cleaned with distilled water quite a few times, consequently it was dried at 180 °C in hot air oven for about 2 h and then it was examined for four successive runs under the same conditions. The catalytic transition of glycerol and selectivity of formic acid decreased from 97.3% to 77.7% and 95.3% to 74.9%, respectively. This may be due to the mass loss which has occurred during the catalyst washing and recovery procedures [46, 47].

Reaction Pathway

Scheme 1 shows the probable reaction mechanism for the catalytic oxidation of glycerol to formic acid. In the initial stage glycerol is oxidized to form either glyceraldehyde or dihydroxyacetone. On further losing an electron, glyceraldehyde forms glyceric and tartronic acid. Subsequently the glyceric acid experiences rapid C–C bond cleavage to form glycolic acid and formaldehyde, which on further oxidation to forms the formic acid [48, 49].



Scheme 1 Possible reaction pathway for glycerol oxidation over Zn²⁺ ($x=0.5$) doped Co₃O₄ catalyst

Conclusion

Microwave assisted combustion technique was used to successfully synthesize Zn²⁺ doped Co₃O₄ spinel nanoparticles. Undoped cobalt oxide and zinc doped cobalt oxide ($x=0.1$ and 0.2) all exhibited a single-phase spinel with a cubic structure. Increase in doping ($x \geq 0.5$), a new hexagonal phase was occurred with addition of cubic structure. Zn²⁺ doping into Co₃O₄ is observed to induce a negative shift in the flat-band potential and increase the isoelectric point. FT-IR study further confirms the bands at 662 and 573 cm⁻¹, spinel cubic and hexagonal stretching modes, respectively. It is noted that with the increase of Zn²⁺ concentration, results in reduced band gap value. HR-TEM and SEM observations reveal that, the homogeneous distribution of Zn²⁺ in Co₃O₄ with high-quality lattice fringes. The existence of Zn, Co, and O was verified by EDX analysis. Depending on Zn²⁺ doping concentration, para-to-super-paramagnetic behavior is observed, combined with a significant difference in the magnetic parameters. Zn²⁺ doped Co₃O₄ spinel

nanoparticles act as a suitable compound for the selective liquid phase conversion of glycerol to formic acid, exhibiting high conversion and selectivity more than 95%.

Supplementary Information The online version contains supplementary material available at <https://doi.org/10.1007/s10876-022-02369-5>.

Acknowledgements The authors (R. Jothi Ramalingam and Hamad Al-Lohedan) are grateful to Deanship of Scientific research, King Saud University for financial support through vice Deanship of Research Chair, Research Chair of Surfactant.

References


- G. V. M. Williams, T. Prakash, J. Kennedy, Shen V. Chongc, and S. Rubanov (2018). *J. Magn. Magn. Mater.* **460**, 229–233.
- M. Sukumar, L. J. Kennedy, J. J. Vijaya, B. Al-najar, and M. Bououdina (2018). *J. Magn. Magn. Mater.* **465**, 48–57.
- H. B. Duvuru, S. K. Alla, S. K. Shaw, S. S. Meena, N. Gupta, B. B. V. S. Vara Prasad, M. M. Kothawale, M. K. Kumar, and N. K. Prasad (2019). *Ceram. Int.* **45**, 16512–16520.
- Ed Lester, Gabriele Aksomaityte, Jun Li, Sara Gomez, Jose Gonzalez-Gonzalez, Martyn Poliakov (2012). *Prog. Cryst. Growth Charact. Mater.* **58**, 3–13.
- F. Manteghi, S. H. Kazemi, M. Peyvandipoor, and A. Asghari (2015). *RSC Adv.* <https://doi.org/10.1039/C5RA09060A>.
- N. M. Dang, W.-W. Zhao, H. N. Shin-ichi Yusa, and K. Nakashima (2015). *New J Chem.* <https://doi.org/10.1039/c5nj00058k>.
- L. Qiao, H. Y. Xiao, H. M. Meyer, J. N. Sun, C. M. Rouleau, A. A. Poretzky, D. B. Geohegan, I. N. Ivanov, M. Yoon, W. J. Weber, and M. D. Biegalski (2013). *J. Mater. Chem. C* **1**, 4628.
- Damian C. Onwudiwe, Murendeni P. Ravele, and Elias E. Elemike (2020). *Nano-Structures & Nano-Objects* **23**, 100470.
- C. S. Jincy and P. Meena (2020). *Inorg. Chem. Commun.* **120**, 108145.
- A. S. Bhatt, D. K. Bhat, C.-w. Tai, and M. S. Santosh (2011). *Mater Chem. Phys.* **125**, 347–350.
- R. Sukhin Saravan, M. Muthukumar, M. Mubashera, M. Abinaya, P. VarunPrasath, R. Parthiban, F. Mohammad, W. C. Oh, and S. Sagadevan (2020). *Opt Opt.* <https://doi.org/10.1016/j.ijleo.2020.164428>.
- H. Wang, L. Zhang, X. Tan, et al. (2011). *J. Phys. Chem. C* **115**, 17599–17605.
- B. Yan, L. Chen, Y. Liu, et al. (2014). *Cryst Eng Comm.* **16**, 10227–10234.
- Y. Lü, W. Zhan, Y. He, et al. (2014). *ACS Appl. Mater. Interfaces* **6**, 4186–4195.
- L. Chen, J. Hu, R. Richards, S. Prikhodko, and S. Kodambaka (2011). *Nanoscale* **2**, 1657–1660.
- R. Gao, Z. Yang, L. Zheng, G. Lin, L. Liu, Y. Lee, H. Zhongbo, and X. Liu (2018). *ACS Catal.* **8** (3), 1955–1963.
- A. M. El Sayed and S. El-Gamal (2015). *J. Polym. Res.* **22**, 97.
- L. Armelao, D. Barreca, S. Gross, and E. Tondello (2001). *Surf. Sci. Spectra* **8**, 14.
- R. V. Kumar, Y. Diamant, and A. Gedanken (2000). *Chem. Mater.* **12**, 2301.
- V. Patil, P. Joshi, M. Chougule, and S. Sen (2012). *Soft Nanosci. Lett.* **2**, 1–7.
- S. G. Victoria, A. M. E. Raj, and C. Ravidhas (2015). *Mater. Chem. Phys.* **162**, 852–859.
- M. Goudarzi, M. Bazarganipour, and M. Salavati-Niasari (2014). *RSC Adv.* **4**, 46517.

23. X. Wang, X. Y. Chen, L. S. Gao, H. G. Zheng, Z. Zhang, and Y. T. Qian (2004). *J. Phys. Chem. B* **108**, 16401.
24. S. A. Makhlouf, Z. H. Bakr, K. I. Aly, and M. S. Moustafa (2013). *Superlat Microstruct* **64**, 107–117.
25. F. Moro, S. V. Y. Tang, F. Tuna, and E. Lester (2013). *J. Magn. Magn. Mater.* **348**, 1–7.
26. M. Sukumar, L. John Kennedy, J. Judith Vijaya, B. Al-Najar, M. Bououdina, and G. Mudhana (2019). *Vacuum* **167**, 407–415.
27. H. Bindu Duvuru, S. K. Alla, S. K. Shaw, S. S. Meena, N. Gupta, B. B. V. S. Vara Prasad, M. M. Kothawale, M. K. Kumar, and N. K. Prasad (2019). *Ceram. Int* **45**, 16512–16520.
28. Ou. Kai, Shenwei Wang, Yu. Liyuan Bai, K. Z. Wang, and Lixin Yi (2019). *Thin Solid Films* **669**, 247–252.
29. X. Li, Y. Qingjiang, Y. Cuiling, Y. Huang, R. Li, J. Wang, F. Guo, Y. Zhang, S. Gao, and L. Zhao (2015). *J. Mater. Chem. A* **3**, 8076–8082.
30. M. Ahamed, M. Javed Akhtar, M. A. Majeed Khan, M. Z. Alaiz-eri, and H. Alhadlaq (2021). *ACS Omega* **6**, 17353–17361.
31. Luiz C.A. Oliveira, Marcio F. Portilho, Adilson C. Silva, Hosane A. Taroco, Patterson P. Souza (2012). *Appl. Catal. B.*, 117–118, 29–35.
32. M. Sundararajan, L. John, J. J. Kennedy, and U. A. Vijaya (2015). *Spectrochim. Acta Part a Mol. Biomol. Spectrosc.* **140**, 421–430.
33. M. Sukumar, L. John Kennedy, J. Judith Vijaya, B. Al-Najar, and M. Bououdina (2018). *Ceram. Int.* **44**, 18113–18122.
34. M. Sundararajan, J. Vidhya, R. Revathi, M. Sukumar, B. Arunadevi, R. Rajkumar, S. Ramachandran, M. Kamalakannan, Chandra Sekhar Dash, Jothi Ramalingam Rajabathar, and Selvaraj Aroykaraj, *Inorg. Nano-Met.*, DOI: <https://doi.org/10.1080/24701556.2021.2025400>.
35. Mahmoud Nasrollahzadeh, BabakJaleh and AmenehJabbari (2014). *RSC Adv.*, 4, 36713.
36. M. Sukumar, L. J. Kennedy, J. J. Vijaya, B. Al-Najar, and M. Bououdina (2018). *New J. Chem.* **42**, 18128–18142.
37. S. Baskar, S. Yuvaraj, M. Sundararajan, and C. SekharDash (2020). *J Supercond Nov Magn.* <https://doi.org/10.1007/s10948-020-05665-1>.
38. Shan Fan, Wen Wang, Hua Ke, Yu. Jian-Cun Rao, and Zhou, (2016). *RSC Adv.* **6**, 97055–97062.
39. Liangmiao Zhang, Xin Zhao, Wenjing Ma, Wu. Milin, Na. Qian, and Lu. Wencong (2013). *CrystEngComm* **15**, 1389–1396.
40. F. Soofivand (2012). *M. Salavati-Niasari* **5**, 64346–64353.
41. G. A. Babu, G. Ravi, T. Mahalingam, M. Navaneethan, M. Arivanandhan, and Y. Hayakawa (2014). *J. Phys. Chem. C* **118**, 23335–23348.
42. M. Agila and S. Krithiga (2019). *Int. j. eng. sci. manag. res.* **2** (2), 475–482.
43. G. D. Tang, Z. Z. Li, L. Ma, W. H. Qi, L. Q. Wu, X. S. Ge, G. H. Wu, and F. X. Hu (2018). *Phys. Rep.* **758**, 1–56.
44. S. Ramachandran, C. S. Dash, A. Tamilselvan, S. Kalpana, and M. Sundararajan (2020). *J. Nanosci. Nanotechnol.* **20**, 2382–2388.
45. S. Thanasilp, J. W. Schwank, V. Meeyoo, S. Pengpanich, and M. Hunsom (2015). *Chem. Eng. J.* **275**, 113–124.
46. M. Sukumar, L. J. Kennedy, J. J. Vijaya, B. Al-Najar, and M. Bououdina (2019). *Mater. Sci. Semicond. Process.* **100**, 225–235.
47. M. Sukumar and L. John Kennedy (2019). *J. Nanosci. Nanotechnol.* **19**, 826–832.
48. S. Vajíček, M. Štolcová, A. Kaszonyi, M. Mičušík, P. Alexy, P. Canton, G. Onyestyák, S. Harnos, F. Lónyi, and J. Valyon (2016). *J. Ind. Eng. Chem.* **39**, 77–86.
49. G.-Y. Yang, Y.-H. Ke, H.-F. Ren, C.-L. Liu, R.-Z. Yang, and W.-S. Dong (2016). *Chem. Eng. J.* **283**, 759–767.

Publisher's Note Springer Nature remains neutral with regard to jurisdictional claims in published maps and institutional affiliations.

Springer Nature or its licensor (e.g. a society or other partner) holds exclusive rights to this article under a publishing agreement with the author(s) or other rightsholder(s); author self-archiving of the accepted manuscript version of this article is solely governed by the terms of such publishing agreement and applicable law.

Authors and Affiliations

Chandra Sekhar Dash¹ · M. Sukumar²  · V. Ravi³ · G. Anitha⁴ · Jothi Ramalingam Rajabathar^{5,7} · Khadijah Mohammedsaleh Katubi⁶ · Norah Salem Alsaieri⁶ · khamael M. Abualnaja⁷ · R. Rajkumar¹¹ · M. Kamalakannan⁸ · M. Sundararajan⁹ · A. Sutha¹⁰

¹ Department of Electronics and Communication Engineering, Centurion University of Technology and Management, Odisha, Bhubaneswar 752050, India

² Department of Physics, Anand Institute of Higher Technology, Kazhipattur, Chennai 603103, India

³ School of Electronics Engineering, Vellore Institute of Technology, Chennai, Tamilnadu 600 127, India

⁴ Department of Electronics and Communication Engineering, Saveetha School of Engineering, Saveetha Institute of Medical and Technical Sciences, Saveetha University, Chennai, Tamilnadu 602105, India

⁵ Surfactant Research Chair, Chemistry Department, College of Science, King Saud University, P.O. Box 2455, Riyadh 11451, Saudi Arabia

⁶ Department of Chemistry, College of Science, Princess Nourah Bint Abdulrahman University, P. O. Box 84428, Riyadh 11671, Saudi Arabia

⁷ Department of VLSI Microelectronics, Institute of ECE, Saveetha School of Engineering, Saveetha University, Chennai, India

⁸ Department of Basic Sciences, College of Fisheries Engineering, Tamil Nadu Dr. J. Jayalalithaa Fisheries University, Nagapattinam 611 002, India

⁹ PG & Research Department of Physics, Paavendhar College of Arts & Science, M.V. South, Thalavasal, Salem, Tamilnadu 636 121, India

¹⁰ Department of Physics, Panimalar Engineering College, Poonamallee, Chennai, Tamil Nadu 600123, India

¹¹ Department of Electronics and Communication Engineering, Vel Tech Rangarajan Dr Sagunthala R&D Institute of Science and Technology, Chennai, India